RSC Advances

PAPER

View Article Online
View Journal | View Issue

Cite this: *RSC Adv.*, 2026, **16**, 6876

Electrochemical synthesis of polyaniline–Ni–Co hybrid structures on titanium substrates for ultrahigh-capacitance supercapacitor electrodes

Abdullah Wasif, [ac] Md Humayun Kabir, [*b] Md. Ershad Halim,[c] Md. Sanwar Hossain,[a] Fatema Tuz Zohora [ac] and Sabina Yasmin [*a]

Electrodes are crucial for electrochemical supercapacitor performance, and thin-film electrodes with active layers on conductive substrates enable fast ion transport and efficient charge storage, making them ideal for advanced supercapacitor applications. However, achieving high areal capacitance on titanium current collectors with a simple, binder-free process remains challenging. In this work, we fabricate a binder-free PANI–Ni–Co hybrid film on Ti sheets by sequential electrodeposition of a Ni–Co alloy followed by *in situ* electrochemical polymerization of polyaniline. XRD, SEM/EDS, and XPS confirm a finely granular Ni–Co scaffold conformally coated by a porous PANI overlayer. Compared with bare Ti and Ni–Co/Ti, the PANI–Ni–Co/Ti electrode exhibits markedly enhanced charge storage in 1.0 M H_2SO_4. It delivers an areal capacitance of 1230 mF cm^{-2} at 1 mA cm^{-2} from GCD and 2819 mF cm^{-2} at 5 mV s^{-1} from CV, while retaining 272.5 mF cm^{-2} at 10 mA cm^{-2} and ~11% of its low-rate capacitance at 200 mV s^{-1}. Notably, the electrode shows good cycling durability, retaining 81.8% of its initial capacitance after 1000 GCD cycles, and post-cycling CV profiles recorded in the used and refreshed electrolytes remain essentially unchanged, indicating preserved electrochemical integrity. The Ragone analysis shows energy densities up to 0.11 mWh cm^{-2} at 0.4 mW cm^{-2}, decreasing to 0.025 mWh cm^{-2} at 4.0 mW cm^{-2}. EIS reveals reduced solution and charge-transfer resistances and near-ideal capacitive behavior for the hybrid electrode. This simple, room temperature, all electrochemical strategy provides a scalable route to high-areal-capacitance Ti-based electrodes for miniaturized supercapacitors, which are suitable for powering or buffering low-power wearable and microelectronic devices.

Received 20th November 2025
Accepted 12th January 2026

DOI: 10.1039/d5ra08977h

rsc.li/rsc-advances

1. Introduction

In today's rapidly advancing world, the demand for reliable, efficient, and sustainable energy solutions is greater than ever. Energy storage technologies have become essential, effectively bridging the gap between energy generation and consumption.[1] Among electrochemical energy-storage technologies, rechargeable zinc–air batteries and supercapacitors have attracted extensive interest, with recent advances in transition-metal-based air cathodes and defect-engineered pseudocapacitor electrodes significantly improving energy density and cycling durability.[2,3] To meet this growing demand, researchers are developing flexible energy storage systems for lightweight, high-performance portable devices that power diverse applications.[4,5]

In response to evolving energy demands, supercapacitors-renowned for their remarkable power density, rapid charge–discharge rates, enduring cycle life, and user-friendly operation-have emerged as a focal point of research.[6,7] Moreover, the global market is expected to expand at roughly a 30% compound annual growth rate (CAGR), reaching around US $8.3 billion by 2025.[8] Yet, their practical deployment remains constrained by limited capacitance and energy density, which are primarily governed by the intrinsic properties of the electrode materials.[9,10] To overcome these challenges, researchers have focused on developing advanced electrode architectures, such as flexible nanocomposites and hybrid materials, which combine multiple charge-storage mechanisms to achieve ultrahigh capacitance and improved electrochemical performance.[11,12] Therefore, the development of ultracapacitors that are not only flexible and lightweight but also capable of delivering exceptionally high capacitance is crucial for practical energy storage applications and device integration.[13] In practical terms, lithium-ion batteries provide high energy densities (~120–200 Wh kg^{-1}) but only modest power densities.[14] Electrochemical supercapacitors usually offer lower energy densities (1–10 Wh kg^{-1}) but can reach power densities above

[a]*Institute of National Analytical Research and Service (INARS), Bangladesh Council of Scientific and Industrial Research (BCSIR), Dhanmondi, Dhaka-1205, Bangladesh. E-mail: sabinayasmin@bcsir.gov.bd*

[b]*Institute of Food Science and Technology (IFST), Bangladesh Council of Scientific and Industrial Research (BCSIR), Dhanmondi, Dhaka-1205, Bangladesh. E-mail: humayunkabir@bcsir.gov.bd*

[c]*Department of Chemistry, University of Dhaka, Dhaka-1000, Bangladesh*

10^3–10^4 W kg^{-1}.[15] In thin-film or microdevice formats, their areal energy density is often only a few tens of μWh cm^{-2} at milliwatt-level power.[16] As a result, they are mainly used for power buffering or short-term, high-power supply in wearable and microelectronic systems. Therefore, there is a strong need for electrode architectures that increase areal capacitance and energy density while retaining high-rate capability on mechanically robust current collectors such as titanium.

Supercapacitors, also referred to as ultracapacitors or electrochemical capacitors, store energy through electrostatic charge accumulation and redox reactions, utilizing high-surface-area electrodes and thin electrolytic layers to achieve capacitance values that far exceed those of conventional capacitors.[17] There are two primary types of supercapacitors: electrical double-layer capacitors (EDLCs) and pseudocapacitors.[18] While EDLCs offer excellent cycle stability, their energy density remains relatively low.[19] This limitation has directed research toward advanced pseudocapacitors, which employ faradaic charge-transfer processes to enhance energy storage performance.[20] The quest for high-performance pseudocapacitors has since focused on the development of advanced electrode materials that combine high conductivity, rich redox activity, and mechanical robustness for flexible devices.[21]

A critical component in this pursuit is the current collector, which forms the backbone of any electrode. In this context, titanium-based hybrid electrodes have gained increasing attention due to their lightweight nature, high tensile strength, corrosion resistance, and compatibility with compact electronic devices.[22,23] Titanium sheets, in particular, serve as promising current collectors in various energy applications. However, their relatively low electrical conductivity ($\sim 2.38 \times 10^6$ S m^{-1}) compared to metals like copper ($\sim 59.6 \times 10^6$ S m^{-1}) restricts their direct use in high-performance supercapacitors.[24–26] This inherent limitation necessitates the deposition of a highly conductive and electroactive interlayer to enhance charge collection and storage.

To address this limitation, in recent years, transition-metal-based pseudocapacitor materials particularly those based on nickel and cobalt have garnered significant research interest, owing to their superior electrochemical performance, enriched redox activity through multiple oxidation states, natural abundance, lower cost, and relatively low toxicity.[27] The synergistic interaction between Ni and Co ions improves electrochemical activity and facilitates more efficient charge storage.[28] Compared with widely used MnO_2 and Fe_2O_3, which are often limited by low electronic conductivity and sluggish redox kinetics (especially at high rates), Ni–Co benefits from dual redox couples (Ni^{2+}/Ni^{3+} and Co^{2+}/Co^{3+}) and a more conductive charge-transport network, enabling higher pseudocapacitive utilization.[29,30] However, despite their promising electrochemical properties, transition metal-based materials often face critical limitations such as high electrical resistance, relatively low energy density, and insufficient mechanical durability.[13,31,32]

A powerful strategy to overcome these challenges is to integrate a material that provides both high pseudocapacitance and mechanical flexibility. Conducting polymers, and polyaniline (PANI) in particular, have emerged as ideal candidates for this role due to their controllable electrical conductivity, improved crystallinity, ease of synthesis, and high theoretical capacitance.[20,33–36] The combination of a metal oxide and a conducting polymer like PANI can create a synergistic effect, mitigating the individual weaknesses of each component.[37] For example, Muhammad Usman *et al.* synthesized a PANI/Fe–Ni-codoped Co_3O_4 (PANI@FNCO) composite electrode, achieving 1171 F g^{-1} at 1 A g^{-1} and 144 Wh kg^{-1} at 470 W kg^{-1}, with 84% capacitance retention after 2000 cycles.[38] Additionally, Eman A. Alabdullkareem and Junaid Khan reported an $Mn_2P_2O_7$–polyaniline (PMP) hybrid that, as a symmetric device, delivered 79.1 Wh kg^{-1} at 749.3 W kg^{-1} while retaining 90.5% after 10 000 cycles.[39] More broadly, substrate-integrated, binder-free electrodes such as core–shell bimetallic phosphide nanoarrays on 3D scaffolds and Fe/Ni–N–C bifunctional catalysts for Zn–air batteries highlight how architectural design and compositional synergy improve kinetics and durability.[40,41] Building on these promising composites, our work utilizes a highly conductive Ni–Co interlayer on a flexible Ti sheet to further enhance the benefits of PANI, ensuring robust mechanical stability and improved charge transfer for superior flexible supercapacitor performance.

In light of these considerations, this work presents a flexible hybrid electrode materials composed of a titanium sheet modified with a nickel–cobalt (Ni–Co) layer and coated with polyaniline (PANI) through an electrochemical polymerization method, forming a conductive and redox-active surface suitable for high-performance flexible supercapacitors. The PANI–Ni–Co/Ti sheet hybrid electrode demonstrated significantly enhanced electrochemical performance compared to unmodified Ti or individual component systems. This improvement is attributed to the synergistic combination of the redox-active Ni–Co layer and the conductive polyaniline coating, which together offer tunable surface properties, rich pseudocapacitance, and a porous, interconnected structure favorable for ion transport. Moreover, the integration of PANI onto the Ni–Co/Ti sheet substrate notably reduced internal resistance and improved charge transfer characteristics, as evidenced by electrochemical impedance analysis. The electrode also exhibited excellent mechanical flexibility, maintaining stable performance under various bending conditions. These features collectively position the PANI–Ni–Co/Ti sheet electrode as a promising platform for high-performance, flexible supercapacitor applications.

2. Experimental

2.1. Chemicals and reagents

Polyaniline (PANI, ACS reagent, ≥99.5%, CAS: 62-53-3), nickel(II) nitrate hexahydrate ($Ni(NO_3)_2 \cdot 6H_2O$, CAS: 13478-00-7), cobalt(II) nitrate hexahydrate ($Co(NO_3)_2 \cdot 6H_2O$ CAS: 10026-22-9), and 0.1 M boric acid (H_3BO_3, CAS: 10043-35-3) were procured from Merck, Germany. Titanium sheets (thickness: 0.25 mm, 99.7% trace metals basis, CAS: 7440-32-6) were purchased from Sigma-Aldrich, Germany. Hydrochloric acid (37%, CAS: 7647-01-0) and sulfuric acid (95–97%, CAS: 7664-93-9) were obtained

from Sigma-Aldrich, Switzerland. Triton X-100 (laboratory grade, CAS: 9036-19-5) was purchased from Sigma Aldrich in Germany. All reagents were of analytical grade and used without further purification. All aqueous solutions were prepared using ultrapure deionized (DI) water with a specific conductance of less than 0.1 μS cm^{-1}.

2.2. Preparation of PANI–Ni–Co/Ti sheet electrode

In the preparation of the PANI–Ni–Co/Ti sheet electrode, at first the titanium sheet was cut into a 1.6 × 1.6 cm^2 size. The Ti sheet was cleaned using a Triton X-100 solution with sonication for 20 min. Then the Ti sheet was washed with DI water several times and dried at a normal temperature. The Ni–Co solution was made by taking 2.90 g $Ni(NO_3)_2 \cdot 6H_2O$, 2.91 g $Co(NO_3)_2 \cdot 6H_2O$ and 0.62 g H_3BO_3 in a 100 mL volumetric flask to make a 0.1 M solution. 0.1 M aniline solution was prepared using 1.0 M HCl. After preparing the solutions, the Ti sheet was immersed in a 0.1 M Ni–Co solution, followed by electrochemical deposition at an applied potential of −0.8 V for 100 seconds. After deposition, the sheet was rinsed and allowed to dry at room temperature. Subsequently, the dried Ni–Co-modified Ti sheet was placed in a 0.1 M aniline solution, where electrochemical polymerization was carried out at 1.2 V for 300 seconds to deposit the PANI layer. Upon completion of polymerization, the resulting Ni–Co–PANI-modified titanium sheet was thoroughly washed with deionized water and air-dried. The final Ni–Co–PANI/Ti electrode was then prepared for subsequent electrochemical characterization. The preparation process of the modified PANI–Ni–Co/Ti sheet is shown in Scheme 1. The areal mass loading of each deposited layer was quantified gravimetrically as follows:[42]

$$\Gamma = \frac{\Delta m}{A} \left(\text{mg cm}^{-2}\right) \quad (1)$$

where Γ is the areal mass loading, Δm is the deposited mass determined by gravimetry ($\Delta m = m_{after} - m_{before}$), and A is the coated geometric area.

Using the above definition, the mass loading of each electrodeposited layer was determined gravimetrically by weighing the Ti sheet before and after deposition. The coated area on one side was 1.4 × 1.4 cm^2 = 1.96 cm^2; with two-sided deposition, the effective geometric area was A = 3.92 cm^2. The Ni–Co underlayer mass increased from 0.1335 to 0.1339 g, giving Δm_{Ni-Co} = 0.4 mg (Γ_{Ni-Co} = 0.102 mg cm^{-2}). After PANI electropolymerization, the mass increased to 0.1344 g, corresponding to Δm_{PANI} = 0.5 mg (Γ_{PANI} = 0.128 mg cm^{-2}). The total active mass was therefore 0.9 mg and the total mass loading was Γ_{total} = 0.230 mg cm^{-2} on an area of A_{eff} = 3.92 cm^2. The synthesized PANI–Ni–Co/Ti is expected to yield significant areal performance by combining a conductive Ni–Co interlayer that reduces charge-transfer resistance with a thin, conformal two-sided PANI coating that maximizes redox-site utilization and shortens ion-diffusion pathways.

2.3. Characterization of the modified PANI–Ni–Co/Ti sheet and the bare Ti sheet

Crystallographic characteristics were examined *via* X-ray diffraction (XRD) using a SmartLab SE diffractometer (Rigaku, Japan) equipped with a Cu Kα radiation source (λ = 1.541 Å). XRD analysis was employed to identify the crystalline structure and phase composition of the samples. Surface morphology and elemental composition of the bare Ti sheet and the modified PANI–Ni–Co Ti sheet were analyzed using field emission scanning electron microscopy (FESEM) coupled with energy-dispersive X-ray spectroscopy (EDS), utilizing a JEOL JSM-7610F instrument operating within a voltage range of 0.1–30 kV. To investigate surface composition and electronic states, X-ray Photoelectron Spectroscopy (XPS) analyses were performed

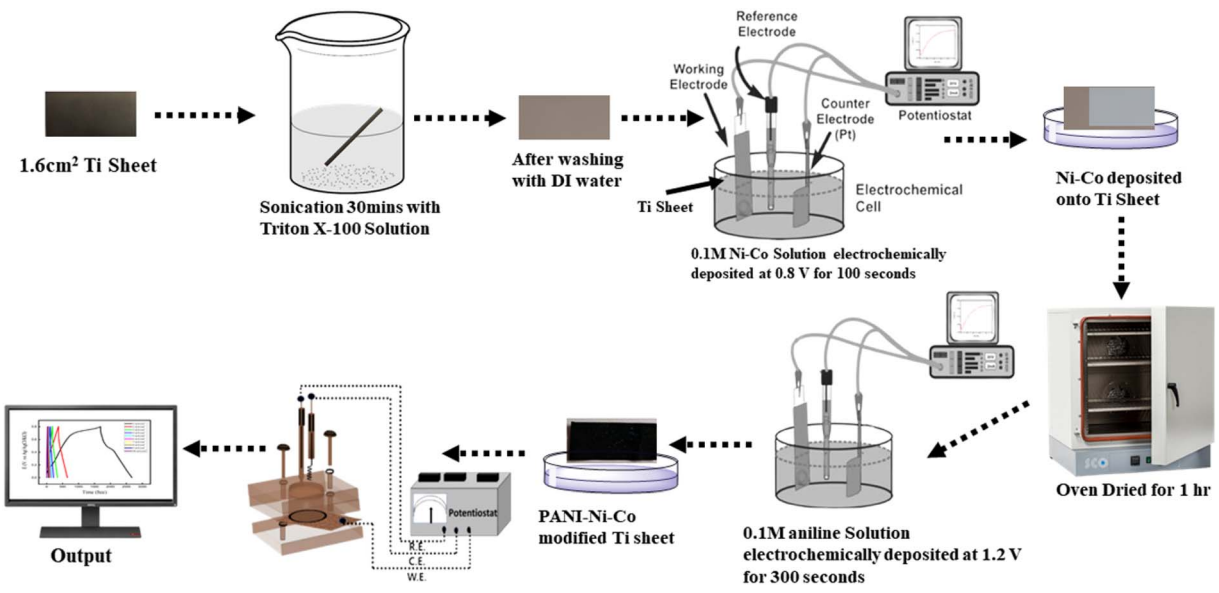

Scheme 1 Schematic representation of the preparation of the modified PANI–Ni–Co/Ti sheet.

by an X-ray Photoelectron spectrometer (Model: K-Alpha, Brand: Thermo Scientific, Country of Origin: Czech Republic) using a monochromatic Al Kα (1486.68 eV) X-ray source, an 180° double-focusing hemispherical analyzer (128-channel 2D detector) and the software named Avantage. The XPS spectra were fitted using a Shirley background, and the peaks were modeled with a mixed Gaussian–Lorentzian function (80% Gaussian and 20% Lorentzian) to ensure accurate spectral representation. The Raman spectra were recorded usinga HORIBAMACRORAM Raman spectrometer, HORIBA Scientific, India. For the electrochemical measurements, a CHI660 workstation (USA) was employed, using a PANI–Ni–Co/Ti sheet as the working electrode, a saturated Ag/AgCl/KCl electrode (CHI111) as the reference, and a platinum wire (BAS Inc., 23 cm) as the counter electrode. Cyclic voltammetry (CV), galvanostatic charge–discharge (GCD), chronoamperometry (CA), and electrochemical impedance spectroscopy (EIS) were conducted to evaluate the electrode performance.

2.4. Electrochemical experiment

All electrochemical studies were conducted in a three-electrode cell, using 1.0 M H_2SO_4 as the electrolyte to evaluate the electrochemical performance. The specific capacitance (C_s), energy density (E), and power density (P) of PANI/Ti sheet electrodes were calculated using eqn (2)–(5):

$$C_s = \frac{It}{A\Delta V} \quad (2)$$

$$E = \frac{C_s \Delta V^2}{2 \times 3600} \quad (3)$$

$$C_{areal} = \frac{\int |I(V)\mathrm{d}v|}{2\nu\ \Delta V A} \quad (4)$$

$$P = \frac{E}{t} \times 3600 \quad (5)$$

where I is the constant discharge current (A), A represents the specific surface area of the electrode (cm^2), t is the discharge time (s), ν is the scan rate, and ΔV denotes the potential window (V).

3. Results and discussion

3.1. X-ray diffraction (XRD) and Raman spectroscopy analysis

X-ray diffraction (XRD) analysis was performed to investigate the crystallographic structure and phase composition of the PANI–Ni–Co/Ti sheet compared to the bare Ti substrate, shown in Fig. 1a. The diffractogram of the bare Ti sheet exhibited characteristic peaks at 2θ values of approximately 38°, 40°, 53°, 70°, and 76°, corresponding to the (110), (101), (200), (220), and (310) crystallographic planes of hexagonal close-packed (hcp) titanium, respectively.[43] After Ni–Co electrodeposition and *in situ* electropolymerization of aniline, the PANI–Ni–Co/Ti pattern retains the strong Ti reflections due to the film being much thinner than the substrate. In addition, film-derived features appear, including a broad PANI diffraction band (amorphous halo) around ~25° and a weak fcc-type Ni–Co (111) signal near 42–43° (COD reference patterns in Fig. 1a).[44,45] Because the Ni–Co layer is very thin compared to the Ti substrate, its signal is weak and overlaps the strong Ti background, so additional Ni–Co reflections are not prominent. The peak-fitting parameters and integrated areas supporting the dominant broad PANI contribution are provided in Table S1. Overall, the diffractograms confirm successful coating while explaining why substrate peaks dominate in this Ti-supported system.

Raman spectroscopy, shown in Fig. 1b further corroborates the formation of a doped polyaniline layer on the Ni–Co-modified Ti substrate. The spectrum is dominated by characteristic PANI backbone vibrations, including the aromatic C=C stretching band at ~1615 cm^{-1}, a quinoid-associated ring stretching feature at ~1500 cm^{-1}, and a prominent polaronic charge-carrier band at ~1345 cm^{-1} assigned to C–N^+.[46] Additional PANI bands are observed at ~1220 cm^{-1} for C–N stretching of benzenoid units, ~1163 cm^{-1} for aromatic C–H in-plane bending, ~1056 cm^{-1} for ring deformation with C–H in-plane bending contributions, ~915 cm^{-1} for ring deformation with C–H out-of-plane contributions, and ~830 and ~765 cm^{-1} for out-of-plane aromatic ring deformations typical of protonated PANI.[47] In the low-wavenumber region, inorganic lattice contributions are evident. A band at ~300 cm^{-1} is attributed to Ni/Co–O lattice vibrations from surface-oxidized Ni/Co species, while features around ~530 cm^{-1} correspond to Ni/Co–O vibrations and may include defect-related contributions depending on oxide disorder.[48,49] Bands in the ~420–460 cm^{-1} range are assigned to Ti–O lattice vibrations associated with the native TiO_2 layer on the Ti current collector.[50] Overall, the coexistence of polaronic PANI signatures above 1000 cm^{-1} with metal–O and Ti–O bands below ~650 cm^{-1} supports the intended multilayer architecture of PANI deposited on a Ni–Co scaffold supported by Ti.

3.2. Scanning electron microscope (SEM) analysis

The surface morphology and elemental composition of the bare Ti sheet, Ni–Co/Ti, and PANI–Ni–Co/Ti electrodes were examined by SEM coupled with EDS. The bare Ti surface (Fig. 2a and b) exhibits the characteristic rolled/striated topography with occasional nanoscale oxide particulates; the roughness map (Fig. 2c) confirms micron-scale relief that provides abundant nucleation sites. Native TiO_2 is evident on the sheet and is corroborated by EDS and XPS (Ti $2p^{4+}$). The presence of TiO_2 on the Ti sheet is due to some Ti particles being oxidized by atmospheric oxygen[51]

After electrodeposition, the Ti surface is conformally coated with a nanogranular Ni–Co layer (Fig. 2d–f). Spherical grains merge into cauliflower-like clusters along steps and valleys, producing a porous, high-surface area structure favorable for charge transfer.[52] EDS (Fig. 2k) detects Ni and Co together with O, consistent with a surface-oxidized/hydroxylated Ni–Co overlayer (representatively ~3.7 at% Ni, ~3.0 at% Co, ~18 at% Ti, balance O).

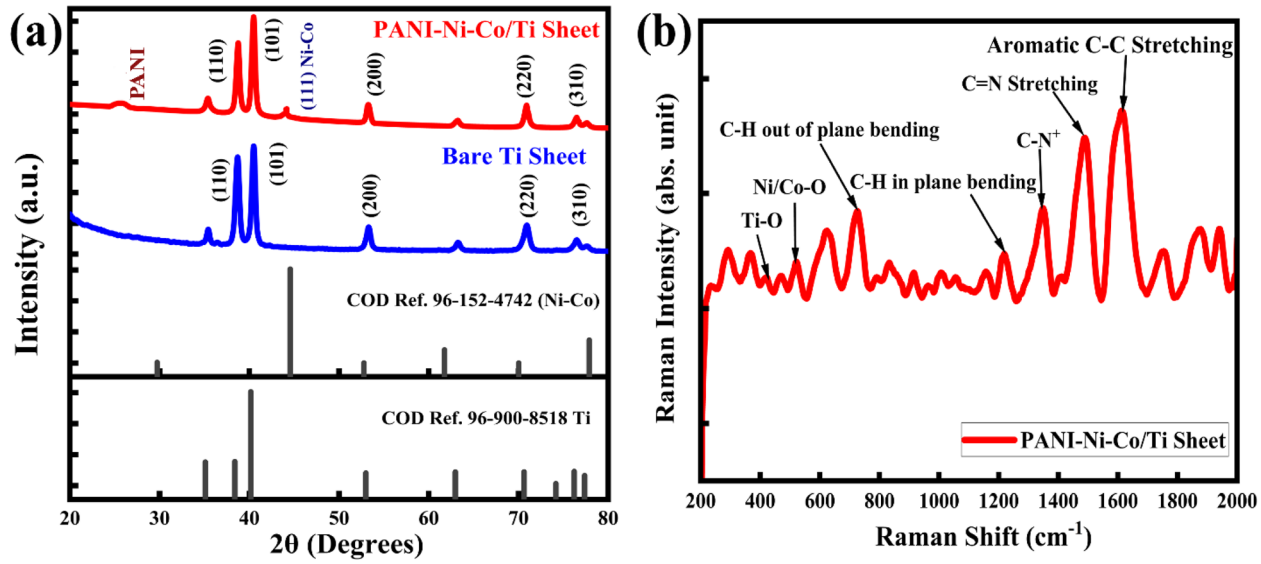

Fig. 1 (a) XRD patterns of bare Ti sheet and PANI–Ni–Co/Ti sheet, with standard/reference patterns for hcp Ti, and fcc Ni–Co for comparison; (b) Raman spectrum of PANI–Ni–Co/Ti sheet with characteristic band assignments.

Subsequent aniline polymerization yields a PANI overlayer on the Ni–Co scaffold (Fig. 2g–i). The polymer rounds the metal granules and forms a continuous, porous skin while preserving interparticle necks and open pathways. Histogram analysis (Fig. 2i) indicates an average particle size of ≈281.7 nm, and this hierarchical porosity is advantageous for supercapacitors by increasing electroactive area and shortening ion diffusion paths.[53,54] EDS of PANI–Ni–Co/Ti (Fig. 2l) shows a marked increase in C with persistent Ni/Co signals and reduced Ti intensity, indicating improved coverage of the alloy by the polymer (*e.g.*, ∼11.2 at% C, ∼27.8 at% Co, ∼7.5 at% Ni, ∼7.1 at% Ti, balance O). Together with XPS (Ni 2p, Co 2p, N 1s), these results confirm the intended multilayer architecture of the textured Ti substrate to a nanogranular Ni–Co scaffold and finally a conformal PANI skin.

3.3. X-ray photoelectron spectroscopy (XPS) analysis

X-ray photoelectron spectroscopy (XPS) confirms the intended PANI–Ni–Co/Ti structure and resolves the surface chemical states (Fig. 3a–g). The survey spectrum (Fig. 3a) displays Ti, Ni, Co, N, O and C, consistent with a PANI overlayer on a Ni–Co film supported by Ti. The spectra were charge-corrected to adventitious C 1s = 284.8 eV and fitted with a Shirley background and mixed Gaussian–Lorentzian components.[55] The C 1s region (Fig. 3b) resolves three principal contributions at ∼284.8 eV (C–C/C–H from the phenyl backbone), ∼286.0 eV (C–N/C–O associated with the polyaniline chain and minor surface hydroxyl/alkoxy), and ∼288.4–288.8 eV (C═O/O–C═O from oxidized carbon).[56–61] The N 1s envelope (Fig. 3c) exhibits the canonical polyaniline signatures: ∼399.0 eV assigned to imine (═N–, quinonoid) nitrogens, ∼400.0–400.2 eV to amine (–NH–, benzenoid) nitrogens, and a higher binding-energy component at ∼401–402 eV from protonated nitrogen (–NH^+), consistent with emeraldine-state PANI; a weak shoulder near ∼399.7–400.0 eV is compatible with interfacial Ti–N/Ti–O–N species created during polymerization.[62–64] The O 1s spectrum (Fig. 3d) contains a lattice oxide peak at ∼529.9–530.2 eV (M–O, primarily TiO_2 and surface-oxidized Ni/Co) and a higher-BE component at ∼531.4–531.8 eV (M–OH/C–O), with a faint tail toward ∼532.6–533.1 eV from adsorbed oxygenated species; these features are consistent with native TiO_2 on the sheet and hydroxylated alloy/PANI interfaces.[65–68] Transition-metal core levels corroborate a surface-oxidized Ni–Co overlayer: Ni 2p (Fig. 3e) shows a main $2p_{3/2}$ line at ∼854.8–855.6 eV accompanied by an intense shake-up satellite near ∼861–862 eV, characteristic of Ni^{2+} ($NiO/Ni(OH)_2$-like), while any metallic Ni^0 (∼852.6 eV) is negligible after air exposure and polymer coating;[69,70] Co 2p (Fig. 3f) presents a $2p_{3/2}$ feature at ∼780.0–780.8 eV with a satellite at ∼786 eV, indicative of Co^{2+} ($CoO/Co(OH)_2$-like), with little or no Co^0 (∼778.1 eV).[71,72] The substrate Ti 2p doublet (Fig. 3g) is centered at ∼458.5 eV ($2p_{3/2}$) and ∼464.2 eV ($2p_{1/2}$), confirming Ti^{4+} in TiO_2; minor lower-BE shoulders (∼455–457 eV) are consistent with interfacial Ti–N/Ti–O–N formed during aniline oxidative polymerization (APS) or at the alloy/Ti interface.[73] Attenuation of Ti 2p relative to the bare sheet, together with the emergence of N 1s and the oxidized Ni/Co states, demonstrates successful polymerization of aniline on the Ni–Co-modified Ti and validates the targeted multilayer architecture. This also rationalizes the Ti-dominated XRD spectra by the nanometric, partially amorphous nature of the surface film.

3.4. Electrochemical performances

The supercapacitive performance of the bare Ti sheet, Ni–Co/Ti sheet, and PANI–Ni–Co/Ti sheet electrodes was evaluated through cyclic voltammetry (CV) analysis in 1.0 M H_2SO_4 at a scan rate of 20 mV s^{-1}, as depicted in Fig. 4a. The PANI–Ni–Co/Ti electrode exhibits a significantly enlarged CV area with

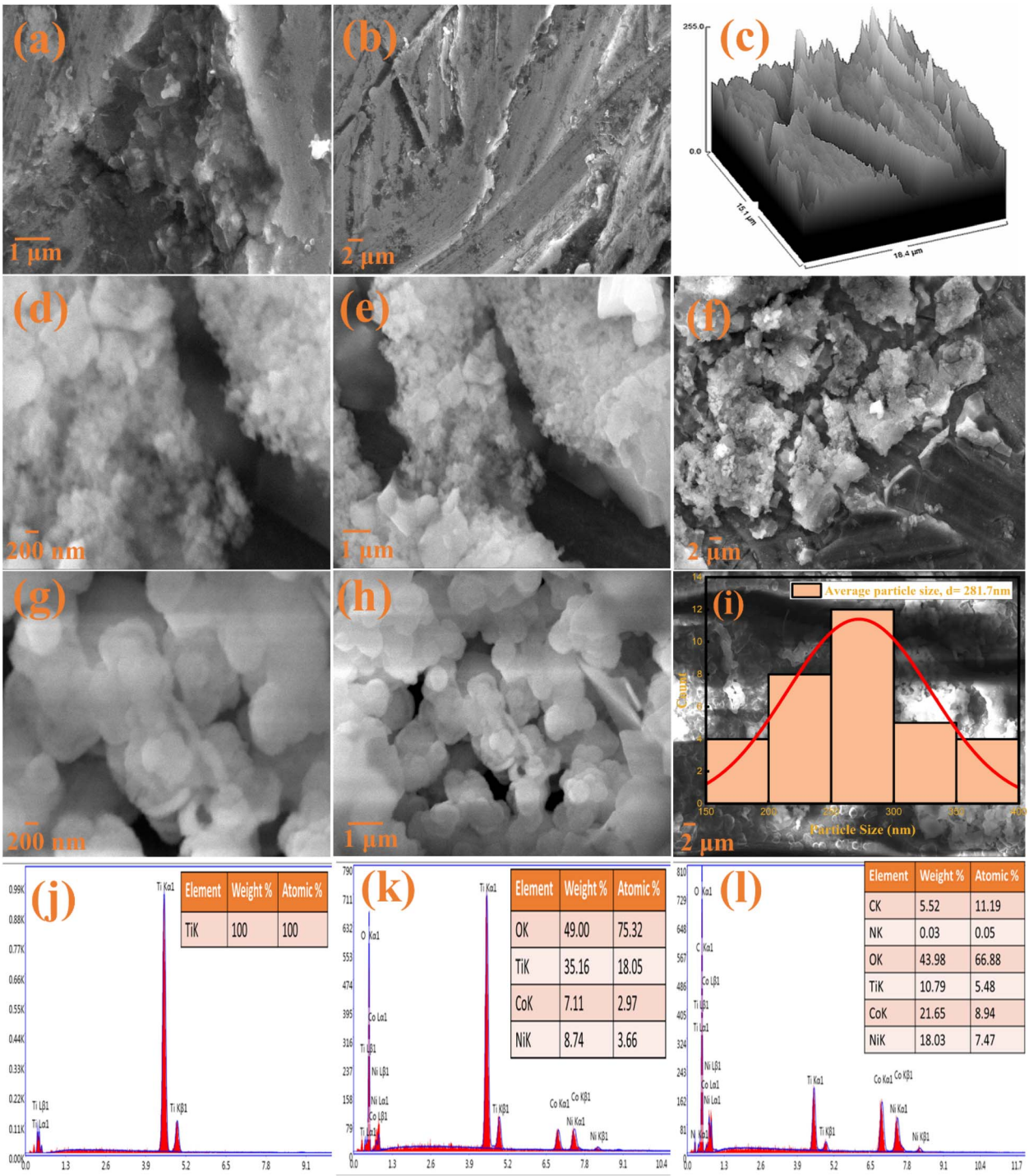

Fig. 2 SEM of (a and b) bare Ti, (c) 3D roughness of Ti; (d–f) Ni–Co/Ti, and (g–i) PANI–Ni–Co/Ti (particle-size in (i): ≈281.7 nm); EDS of (j) Ti, (k) Ni–Co/Ti, and (l) PANI–Ni–Co/Ti.

distinct redox peaks, indicating enhanced pseudocapacitive behavior arising from the faradaic redox reactions of PANI and the Ni–Co layer.[74,75] Polyaniline (PANI) exhibits five distinct oxidation states, with redox transitions typically occurring between the *p*-benzoquinone and hydroquinone units, as well as between the leucoemeraldine and emeraldine forms. Additionally, a notable faradaic transformation takes place from the emeraldine to the pernigraniline oxidation state, contributing significantly to its pseudocapacitive behavior.[76] The quasi-rectangular shape, coupled with the presence of broad redox features, confirms the coexistence of electrical double-layer capacitance and pseudocapacitance.[77] In contrast, the Ni–Co/Ti sheet shows a much smaller enclosed area with minimal redox activity, while the bare Ti sheet demonstrates negligible

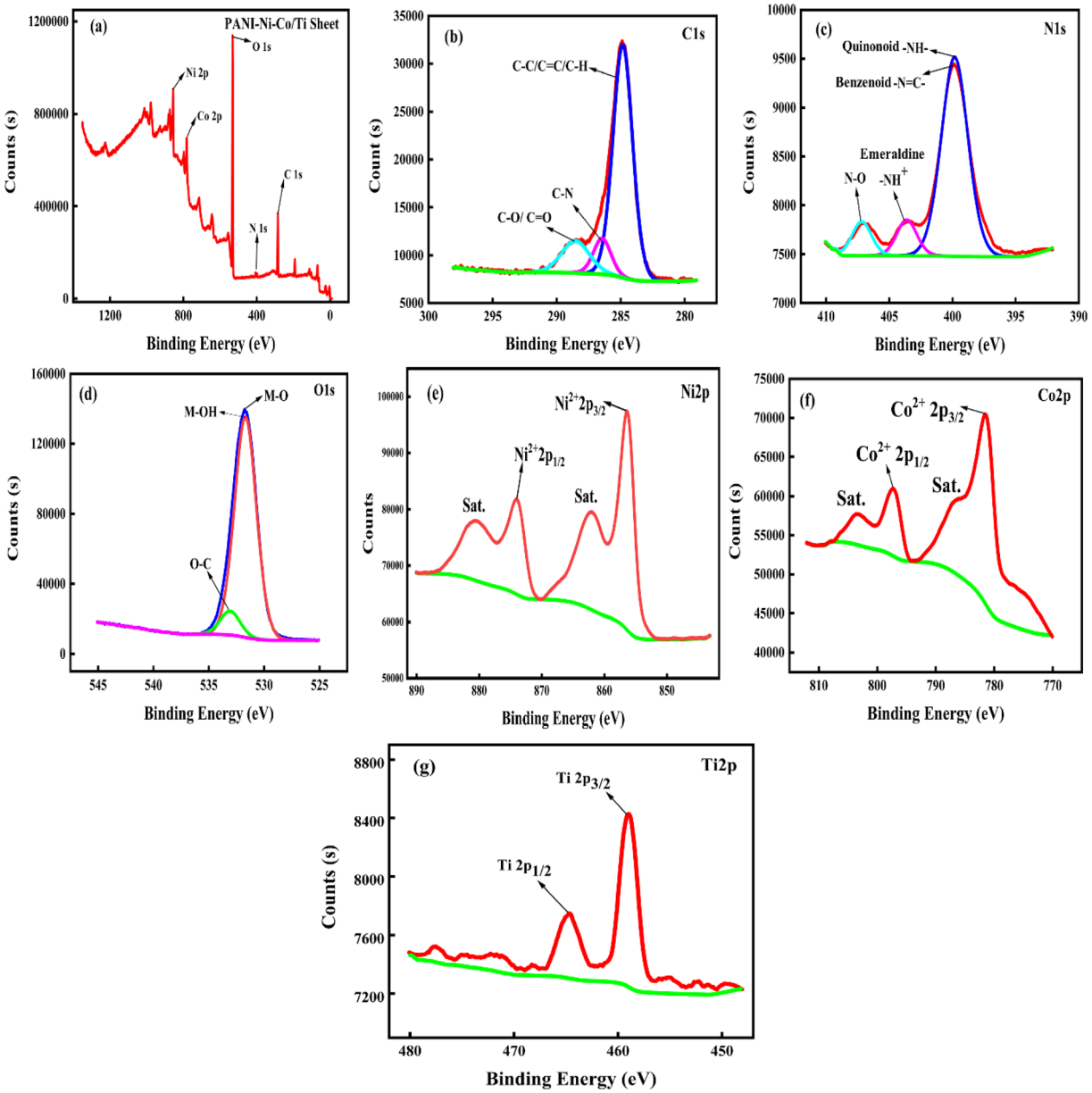

Fig. 3 XPS of PANI–Ni–Co/Ti: (a) survey spectrum of PANI–Ni–Co/Ti sheet (b) C 1s (C–C/C=C, C–N/C=N, C–O), (c) N 1s (–NH–/–N^+=), (d) O 1s (M–O, M–OH, O–C), (e) Ni^{2+} 2p, (f) Co^{2+} 2p with satellites, and (g) Ti 2p from bare Ti sheet.

current response, lacking any capacitive or faradaic features.[78] The areas of CVs for the PANI–Ni–Co/Ti sheet is 26 times greater than that of Ni–Co/Ti sheet and the bare Ti sheet, suggesting the PANI–Ni–Co/Ti sheet can store more charges than the Ni–Co/Ti sheet and the bare Ti sheet. This can be attributed to the synergistic effect between PANI and Ti sheet.[79] The PANI–Ni–Co/Ti sheet shows better capacitance compared to other PANI-modified electrodes, as seen in Table 1. In particular, it delivers a much higher areal capacitance than PANI films on nonporous Au, graphene paper, or TiN-modified Ti foil, which can be ascribed to the rough, conductive Ni–Co interlayer and porous PANI coating that together increase electroactive surface area and reduce interfacial resistance.[80–82] These findings highlight the superior charge storage capability of the PANI–Ni–Co/Ti hybrid electrode, which benefits from both the electroactive polymer and the bimetallic oxide interface.

Fig. 4b compares the GCD curves of the bare Ti sheet, the Ni–Co/Ti sheet (shown in the graphical inset), and the PANI–Ni–Co/Ti sheet recorded at 1 mA cm^{-2} in 1.0 M H_2SO_4. The bare Ti sheet with a specific capacitance of 17.25 mF cm^{-2} delivers a near-ideal electric double-layer response, evidenced by its almost perfectly linear and symmetric charge–discharge profiles and minimal *IR* drop at the onset of discharge, which is consistent with the charge–discharge profiles obtained from literature.[83] In contrast, specific capacitance for the Ni–Co/Ti sheet falls to 9.25 mF cm^{-2}. This behavior aligns with known characteristics of electrodeposited Ni–Co films: dense coatings block conductive substrates, reducing double-layer capacitance

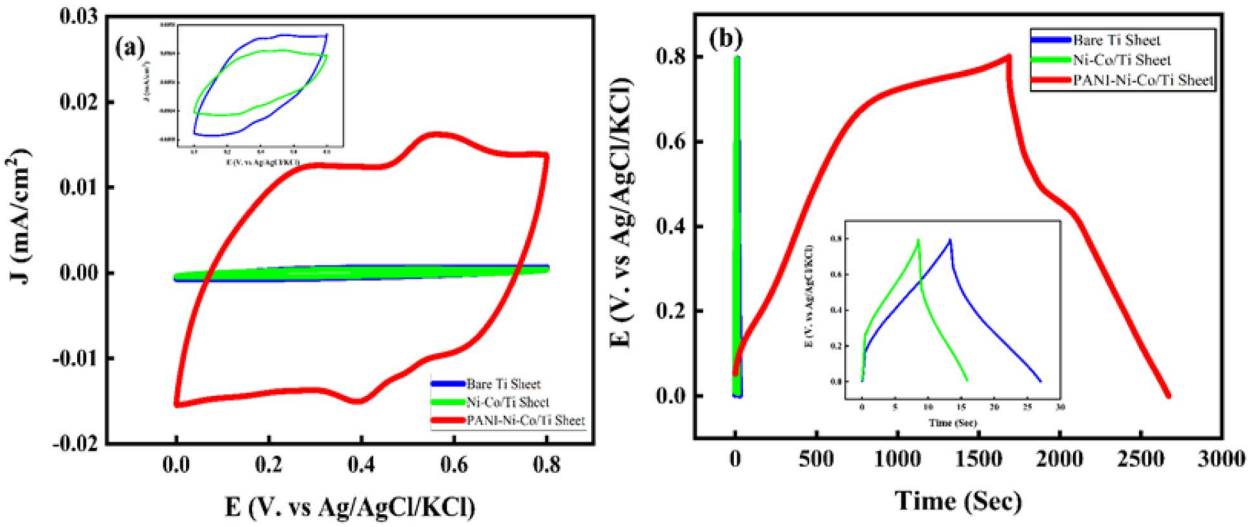

Fig. 4 Electrochemical performance (a) CV and (b) GCD curves of bare Ti sheet, Ni–Co/Ti sheet and PANI–Ni–Co/Ti sheet electrode at 1.0 M H_2SO_4 solution.

and outweighing added pseudocapacitance within the limited voltage window.[84] Now the sheet discharges more quickly and displays a small bend in its profile, indicating a mix of double-layer storage and some pseudocapacitance from redox reactions.[85] The PANI–Ni–Co/Ti sheet stands out with a much longer discharge time and a gently curved slope during both charge and discharge, revealing a strong contribution from polyaniline's faradaic processes and the Ni–Co underlayer. Here, the specific capacitance leaps to 1230 mF cm^{-2}. This performance surpasses comprehensively the PANI-coated nonporous gold (6.54 mF cm^{-2}),[80] PANI-coated graphene paper (123 mF cm^{-2}),[81] and TiN-modified Ti foil (53.66 mF cm^{-2}),[82] highlighting the exceptional charge storage capability of the hierarchically structured hybrid electrode. Based on the comparison of CV and GCD electrochemical performances, the PANI–Ni–Co/Ti sheet was selected as a promising supercapacitor electrode for further electrochemical studies.

The effects of scan rate on the charge storage capacity of the PANI/Ti sheet were investigated. Fig. 5a displays the CVs of the PANI–Ni–Co/Ti sheet in 1.0 M H_2SO_4 at scan rates of 5, 10, 25, 50, 80, 100, 150, and 200 mV s^{-1}. As the scan rate rises, both the anodic and cathodic peak currents grow almost linearly, demonstrating the electrode's strong rate capability.[86] The oxidation peak moves from about 0.48 V at 5 mV s^{-1} to ~0.65 V at 200 mV s^{-1}, while the reduction peak shifts from ~0.18 V down to ~0.04 V at 200 mV s^{-1}. These positive and negative shifts, respectively, reflect the growing influence of internal resistance of the electrode material.[87]

The areal specific capacitance, calculated from the CV curves, exhibited a decreasing trend with increasing scan rate (shown in Fig. 5b), from 2819.4 mF cm^{-2} at 5 mV s^{-1} to 313.7 mF cm^{-2} at 200 mV s^{-1}. This behavior arises from growing kinetic limitations at higher sweep rates: ion diffusion into the porous PANI–Ni–Co network and faradaic charge transfer cannot keep pace, so only near-surface sites contribute and *IR*-drop increases. Even so, the electrode retains ~11% of its low-rate capacitance at 200 mV s^{-1}, reflecting a diffusion-influenced pseudocapacitive system.[88,89]

The relative contributions of capacitive and diffusion-controlled processes were quantified using eqn (6) and (7):[90]

$$i(v) = k_1 v + k_2 v^{\frac{1}{2}} \quad (6)$$

Table 1 Comparison of PANI–Ni–Co/Ti sheet electrode with previously reported substrate-based supercapacitors

	Electrochemical performance				
Material	C_{sp} (mF cm^{-2})	E (mWh cm^{-2})	P (mW cm^{-2})	Retention and cycle (%)	Reference
PANI coated on nonporous gold support	6.54	9.11	1.56		80
PANI-coated graphene paper	123	0.0171	0.25	74.4 after 500 cycles	81
TiN modified Ti foil	53.66	68.70	1.9×10^4	97 after 10 000 cycles	82
Graphene/CNTs	7.7	10.7	3.17	99 after 15 000 cycles	102
TiS_2 aggregate modified Ti foil	136.75	34.35	675.10	96 after 5000 cycles	103
$PC/PAM–PANI_{0.75}$	620	0.0319	0.75	80.7	104
TiO_2@PANI core–shell nanowires	520.3			97.2 after 10 000 cycles	105
PANI–Ni–Co/Ti sheet	**1230**	**0.109**	**4**	**81.8 after 1000 cycles**	**This work**

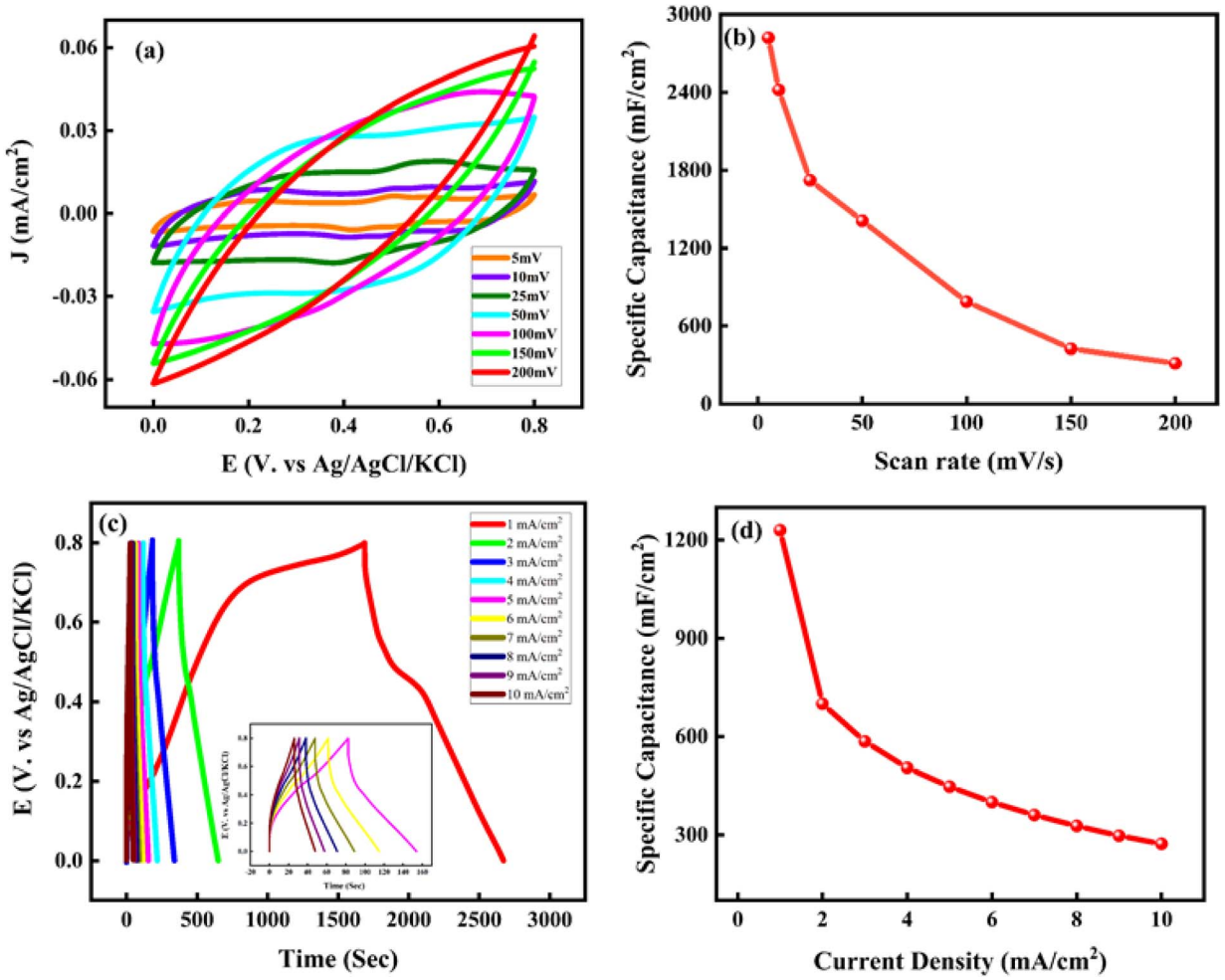

Fig. 5 Electrochemical performance (a) CV curves of PANI–Ni–Co/Ti sheet electrode at various scan rates (5–200 mV); (b) areal capacitance at different scan rates; (c) GCD curves at different current densities (1–10 mA cm^{-2}); (d) areal capacitance at different current densities.

$$\frac{i(\nu)}{\nu^{\frac{1}{2}}} = k_1\nu^{\frac{1}{2}} + k_2 \quad (7)$$

where $k_1\nu$ and $k_2\nu^{1/2}$ represent the capacitive and diffusion-controlled (faradaic) components, respectively. The constants k_1 and k_2 were obtained from the linear fit of $i(\nu)$ *versus* $\nu^{1/2}$ at a fixed potential, as shown in Fig. S1(a) ($k_1 = 0.227$, $k_2 = 0.073$). Fig. S1(b) summarizes the separated contributions at different scan rates.[91,92] As shown in Fig. S1(b), the faradaic (diffusion-controlled) contribution increases from 50.26% at 100 mV s^{-1} to 81.88% at 5 mV s^{-1}, indicating that slower scans allow deeper electrolyte penetration and more complete utilization of redox-active sites within the PANI–Ni–Co network. Conversely, the capacive contribution increases with scan rate (49.74% at 100 mV s^{-1}), consistent with increasingly surface-controlled charge storage when the timescale limits ion diffusion and bulk redox participation. Overall, this scan-rate-dependent partitioning confirms a predominantly pseudocapacitive electrode in which diffusion-governed faradaic reactions dominate at low rates, while surface-controlled processes become more prominent under rapid charging conditions.

GCD (galvanostatic charge–discharge) curves for the PANI–Ni–Co/Ti sheet were recorded at various current densities ranging from 1 to 10 mA cm^{-2} within a voltage window of 0.0 to 0.8 V, as illustrated in Fig. 5c. The main plot shows data for lower current densities (1–4 mA cm^{-2}), while higher current density curves (5–10 mA cm^{-2}) are presented in the inset for clarity. Incorporating PANI with Ni and Co on the surface of the Ti sheet, all GCD profiles exhibit pronounced pseudocapacitive behavior, characterized by non-linear and asymmetric shapes instead of the ideal triangular profiles associated with electric double-layer capacitance. The discharge time decreases significantly with increasing current density, a trend attributed to reduced ion diffusion and active site accessibility at higher charge rates.[93] Notably, the GCD curves display good symmetry between charging and discharging segments, indicating high coulombic efficiency and reversible electrochemical processes. Furthermore, minimal *IR* drop at the start of discharge implies low internal resistance and excellent conductivity of the composite electrode.[94] The calculated C_{sp} of the PANI/Ti sheet reaches 1230 mF cm^{-2} at 1 mA cm^{-2} to 272.5 mF cm^{-2} at 10 mA cm^{-2} (Fig. 5d). Even at higher current densities, the capacitance

remains substantial, reflecting good rate capability and retention. The C_{sp} of PANI–Ni–Co/Ti sheet at 1 mA cm^{-2} is 71.3 times that of a bare Ti sheet and 132.98 times that of the Ni–Co/Ti sheet, respectively. The retention of C_{sp} even at higher current densities indicates the promising potential of the prepared electrode for practical application.

The Ragone plot of the PANI–Ni–Co/Ti sheet, shown in Fig. 6a, illustrates the relationship between energy density and power density, serving as a crucial metric for evaluating the performance of electrochemical energy storage devices.[95] The electrode achieves a maximum energy density of approximately 0.11 mWh cm^{-2} at a low power density of 0.4 mW cm^{-2}, indicating its strong capability to store energy when discharged slowly. As the power density increases to 4.0 mW cm^{-2}, the energy density gradually decreases to 0.025 mWh cm^{-2}. The energy and power density of the prepared electrode were calculated following eqn (3) and (5). This decrease in energy density is a typical trend observed in pseudocapacitive materials due to reduced ion diffusion time and incomplete utilization of electroactive sites at high current rates.[96,97] Despite this, the electrode maintains a relatively stable energy density across a wide power range, highlighting its good rate performance. These characteristics confirm that the PANI–Ni–Co/Ti electrode possesses a favorable balance between high energy and high power output, making it a promising candidate for next-generation supercapacitor applications.

Continuous GCD cycling was conducted to evaluate long-term durability of the PANI–Ni–Co/Ti electrode in 1.0 M H_2SO_4 within 0.0–0.8 V (*vs.* Ag/AgCl) at 10 mA cm^{-2} for 1000 cycles (Fig. 6c). The electrode demonstrates stable cycling

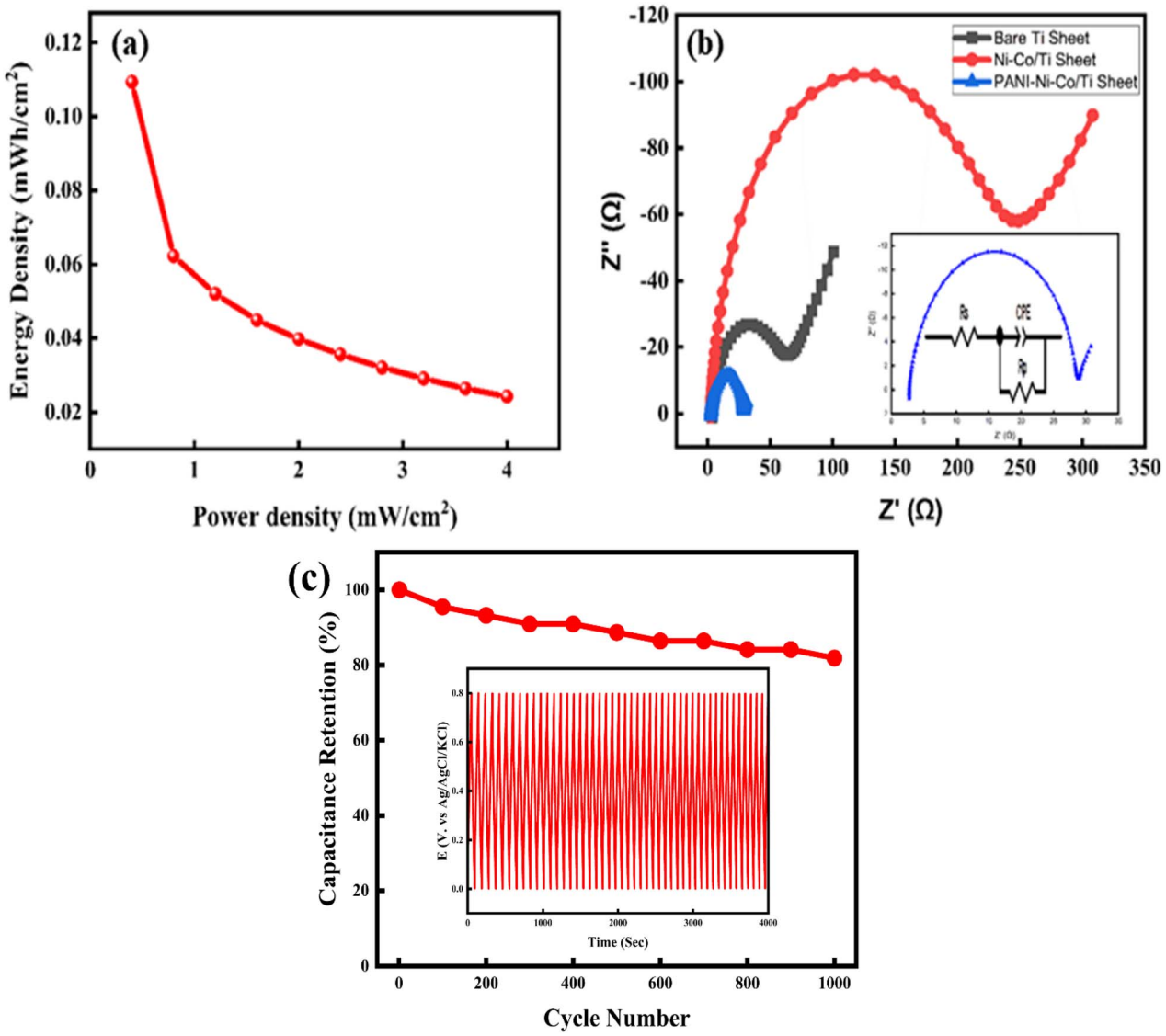

Fig. 6 (a) Ragone plot for PANI–Ni–Co/Ti sheet electrode at 1 M H_2SO_4; (b) Nyquist plots of bare Ti sheet, Ni–Co/Ti sheet, and PANI–Ni–Co/Ti sheet obtained by applying a 5 mV signal amplitude with a frequency range from 0.1 Hz to 10 kHz, (inset) Equivalent circuit diagram used for fitting of the PANI–Ni–Co/Ti sheet. (c) Cycling stability of the PANI–Ni–Co/Ti electrode measured by GCD at 10 mA cm^{-2} in 1.0 M H_2SO_4 within 0.0–0.8 V (*vs.* Ag/AgCl) for 1000 cycles. Inset: representative charge–discharge profiles during cycling.

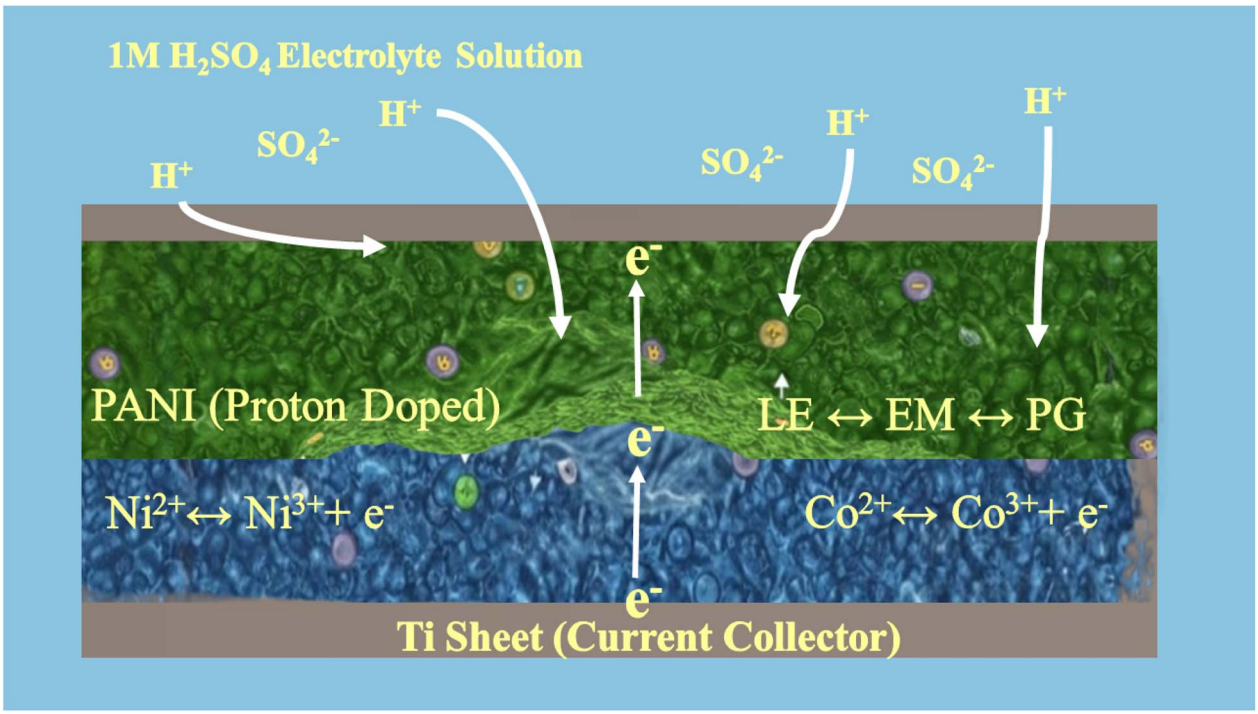

Fig. 7 Schematic illustration of the charge-storage mechanism and Ni–Co/PANI synergy in 1.0 M H_2SO_4.

behavior, retaining 81.8% of its initial areal capacitance after 1000 cycles, with the capacitance decreasing from ~550 mF cm^{-2} (cycle 1) to ~450 mF cm^{-2} (cycle 1000). The charge–discharge traces remain quasi-symmetric throughout cycling (inset of Fig. 6c), reflecting good reversibility. To confirm post-cycling integrity, CV curves recorded at 20 mV s^{-1} after cycling using the existing electrolyte and after replacement with fresh electrolyte show largely preserved CV shapes (Fig. S3), indicating that the hybrid electrode maintains its charge-storage mechanism after prolonged cycling.

To quantify the electrochemically accessible surface area, ECSA was estimated from the double-layer capacitance using eqn (8):

$$\text{Roughness factor} = \frac{C_{dl}}{C_s} \quad (8)$$

where C_s is the specific capacitance of a smooth planar surface. For the PANI–Ni–Co/Ti sheet electrode, C_s was taken as 40 μF cm^{-2}[98] with C_{dl} = 0.2476 mF cm^{-2}, the corresponding roughness factor (C_{dl}/C_s) is 6.19, which means the electrochemically active surface area is 6.19 times greater than the geometrical area.

Electrochemical impedance spectroscopy (EIS) was used to elucidate the interfacial kinetics of the three electrodes in 1.0 M H_2SO_4 (5 mV AC; 10^5–10^{-1} Hz).[99] The Nyquist overlays (Fig. 6b) show a single depressed semicircle at high–mid frequencies and, for Ni–Co/Ti, a clear low-frequency rise, whereas PANI–Ni–Co/Ti displays the smallest arc and only a faint tail. The high-frequency intercepts indicate the ohmic drop (R_s): bare Ti ≳ Ni–Co/Ti > PANI–Ni–Co/Ti, consistent with improved current collection in the polymer-modified electrode. Quantitative fitting of the PANI–Ni–Co/Ti data with a Randles-type circuit reproduces the full semicircle (visual diameter ≈26.15 Ω; low intercept ≈2.81 Ω) and yields R_s = 2.86 Ω, R_p = 25.32 Ω, and a nearly ideal interfacial capacitance (CPE-T = 1.47 × 10^{-5} s^n Ω^{-1}, n = 0.951), evidencing modest dispersion from surface heterogeneity. The associated kinetic time constant $\tau \approx R_p \times T$ is 3.7 × 10^{-4} s, giving a corner frequency $f_c \approx 1/(2\pi\tau) \approx$ 430 Hz, in agreement with the phase maximum. In contrast, Ni–Co/Ti exhibits a much larger arc and a pronounced diffusion feature at low frequency (finite-length/Warburg behavior), signifying higher charge-transfer polarization and slower mass transport within the metal-only scaffold. Collectively, the markedly lower R_s and reduced R_p of PANI–Ni–Co/Ti, together with its near-ideal capacitive response, corroborate that the polymer-coated alloy furnishes faster interfacial electron transfer and more facile ion access, mechanistic factors that align with its superior CV/GCD performance.

On the basis of the above structural and electrochemical analyses, the charge-storage behaviour of the PANI–Ni–Co/Ti electrode is governed by a mixed but pseudocapacitance-dominated mechanism (shown in Fig. 7). In 1.0 M H_2SO_4, the PANI overlayer stores charge *via* fast proton-coupled redox transitions between its leucoemeraldine, emeraldine and pernigraniline states, providing surface-confined pseudocapacitance. At the same time, the Ni/Co species in the alloy underlayer, which is partially converted to surface (oxy)hydroxides, participate in reversible Ni^{2+}/Ni^{3+} and Co^{2+}/Co^{3+} transitions at the electrode/electrolyte interface, further contributing to charge storage and lowering the charge-transfer resistance. Taken together, the multivalent Ni–Co redox scaffold provides

abundant faradaic centers,[100] while the redox-active PANI overlayer promotes rapid charge transport and interfacial kinetics. This cooperative coupling increases redox-site utilization and suppresses polarization (lower R_s/R_p), thereby accounting for the markedly enhanced areal capacitance of the hybrid electrode.[101] The Ti substrate mainly serves as a mechanically robust current collector with minor double-layer contribution at the TiO_2 and polymer interfaces. The quasi-rectangular CV profiles with broad redox features, non-linear GCD curves, and the low R_s and R_p values extracted from EIS together confirm this synergistic pseudocapacitive energy-storage mechanism for the PANI–Ni–Co/Ti hybrid electrode.

4. Conclusion

In this study, a hybrid electrode comprising Ni–Co and polyaniline (PANI) was successfully fabricated on titanium substrates *via* sequential electrodeposition and *in situ* polymer growth. The Ni–Co scaffold facilitates rapid electron transport, while PANI provides abundant and fast redox-active sites, resulting in significantly enhanced performance compared to bare Ti and Ni–Co/Ti electrodes. The PANI–Ni–Co/Ti electrode achieves an ultrahigh areal capacitance of 1230 mF cm^{-2} at 1 mA cm^{-2}, retaining 272.5 mF cm^{-2} at 10 mA cm^{-2}, and demonstrates excellent rate capability, maintaining 2819–313 mF cm^{-2} across scan rates from 5 to 200 mV s^{-1}. The synergistic combination of the Ni–Co scaffold and PANI offers a generalizable strategy for developing high-areal-capacitance thin films with other metal–polymer systems. These findings establish PANI–Ni–Co/Ti as a mechanically robust, high-performance platform for next-generation supercapacitors.

Conflicts of interest

There are no conflicts to declare.

Data availability

The authors do not have permission to share data.

Supplementary information (SI) is available. See DOI: https://doi.org/10.1039/d5ra08977h.

Acknowledgements

The authors are grateful to the Bangladesh Council of Scientific and Industrial Research (BCSIR) for financial support (R&D ref. no. 39.02.0000.011.14.180.2024/1116, date:14.01.2025) and facilities.

References

1 N. McIlwaine, A. M. Foley, D. J. Morrow, D. A. Kez, C. Zhang, X. Lu and R. J. Best, *Energy*, 2021, **229**, 120461.
2 Q. Sun, K. Li, T. Shu, Z. Guo, Y. Li, Y. Zhang, L. Li, J. Ning, P. Zhao and K. X. Yao, *Chem. Eng. J.*, 2025, **516**, 164075.
3 K. Li, Y. Xiao, T. Zheng, Q. Sun, Y. Zhang, H. Teng, W. Wang, K. Yao, J. Rao and Y. Zhang, *Appl. Surf. Sci.*, 2023, **622**, 156950.
4 J. He, L. Cao, J. Cui, G. Fu, R. Jiang, X. Xu and C. Guan, *Adv. Mater.*, 2024, **36**, 2306090.
5 F. Liu, S. Luo, D. Liu, W. Chen, Y. Huang, L. Dong and L. Wang, *ACS Appl. Mater. Interfaces*, 2017, **9**, 33791–33801.
6 G. Smdani, M. R. Islam, A. N. Ahmad Yahaya and S. I. Bin Safie, *Energy Environ.*, 2023, **34**, 1094–1141.
7 D. Liu, X. Wang, J. Deng, C. Zhou, J. Guo and P. Liu, *Nanomaterials*, 2015, **5**, 1034–1047.
8 D. Lasrado, S. Ahankari and K. K. Kar, in *Handbook of Nanocomposite Supercapacitor Materials III: Selection*, ed. K. K. Kar, Springer International Publishing, Cham, 2021, pp. 329–365.
9 L. M. Da Silva, R. Cesar, C. M. R. Moreira, J. H. M. Santos, L. G. De Souza, B. M. Pires, R. Vicentini, W. Nunes and H. Zanin, *Energy Storage Mater.*, 2020, **27**, 555–590.
10 F. T. Zohora, A. Wasif, A. Hussain, M. J. Alam, T. Debnath and Md. E. Halim, *J. Mol. Struct.*, 2026, **1349**, 143634.
11 X. Li, G. Wang, X. Wang, X. Li and J. Ji, *J. Mater. Chem. A*, 2013, **1**, 10103–10106.
12 Y. He, W. Chen, X. Li, Z. Zhang, J. Fu, C. Zhao and E. Xie, *ACS Nano*, 2013, **7**, 174–182.
13 M. S. Hossain, M. H. Kabir, M. A. A. Shaikh, M. Y. Pabel and S. Yasmin, *Mater. Chem. Phys.*, 2024, **322**, 129586.
14 T. Placke, R. Kloepsch, S. Dühnen and M. Winter, *J. Solid State Electrochem.*, 2017, **21**, 1939–1964.
15 A. Du Pasquier, I. Plitz, S. Menocal and G. Amatucci, *J. Power Sources*, 2003, **115**, 171–178.
16 C. Gao, J. Huang, Y. Xiao, G. Zhang, C. Dai, Z. Li, Y. Zhao, L. Jiang and L. Qu, *Nat. Commun.*, 2021, **12**, 2647.
17 M. S. Halper and J. C. Ellenbogen, *Supercapacitors: A Brief Overview*, The MITRE Corporation, McLean, Virginia, USA, 2006.
18 H. Ji, X. Zhao, Z. Qiao, J. Jung, Y. Zhu, Y. Lu, L. L. Zhang, A. H. MacDonald and R. S. Ruoff, *Nat. Commun.*, 2014, **5**, 3317.
19 J. P. Zheng, *J. Electrochem. Soc.*, 2005, **152**, A1864.
20 J. Banerjee, K. Dutta, M. A. Kader and S. K. Nayak, *Polym. Adv. Technol.*, 2019, **30**, 1902–1921.
21 S. Mahala, K. Khosravinia and A. Kiani, *J. Energy Storage*, 2023, **67**, 107558.
22 L. A. Wehner, N. Mittal, T. Liu and M. Niederberger, *ACS Cent. Sci.*, 2021, **7**, 231–244.
23 Y. Xiao, G. Han, H. Zhou and J. Wu, *RSC Adv.*, 2016, **6**, 2778–2784.
24 E. A. Bel'skaya and E. Yu Kulyamina, *High Temp.*, 2007, **45**, 785–796.
25 A. A. Eze, T. Jamiru, E. R. Sadiku, M. Olayinka Durowoju, W. K. Kupolati, I. D. Ibrahim, B. A. Obadele, P. A. Olubambi and S. Diouf, *J. Alloys Compd.*, 2018, **736**, 163–171.
26 R. Y. Sumaiya, S. A. Chhanda, A. Wasif, F. T. Zohora, K. Akhter, Md. S. Islam, N. Uddin and Md. E. Halim, *J. Mol. Struct.*, 2026, **1355**, 145000.

27 C. Wang, P. Sun, G. Qu, J. Yin and X. Xu, *Chin. Chem. Lett.*, 2018, **29**, 1731–1740.
28 H. Chen, S. Chen, Y. Zhu, C. Li, M. Fan, D. Chen, G. Tian and K. Shu, *Electrochim. Acta*, 2016, **190**, 57–63.
29 M. P. Chavhan, S. R. Sethi and S. Ganguly, *J. Energy Storage*, 2020, **32**, 101851.
30 D. Merum, R. K. Chava and M. Kang, *Nanomaterials*, 2025, **15**, 1559.
31 M. Cui and X. Meng, *Nanoscale Adv.*, 2020, **2**, 5516–5528.
32 N. T. Dipannita, S. Yasmin, M. K. Hasan, M. S. Hossain, M. A. Somapti and M. H. Kabir, *RSC Adv.*, 2025, **15**, 35219–35232.
33 M. Mupit, M. R. Islam, M. A. Azam, R. Yunus and O. S. Kooi, *Energy Environ.*, 2024, **35**, 1987–2007.
34 Y. Zou, R. Liu, W. Zhong and W. Yang, *J. Mater. Chem. A*, 2018, **6**, 8568–8578.
35 R. D. Pyarasani, T. Jayaramudu and A. John, *J. Mater. Sci.*, 2019, **54**, 974–996.
36 M. G. Sumdani, M. R. Islam, A. N. A. Yahaya and S. I. Safie, *Polym. Eng. Sci.*, 2022, **62**, 269–303.
37 A. Yadav, H. Kumar, R. Sharma, R. Kumari, D. Singh and O. A. Hamed, *Results Eng.*, 2023, **18**, 101161.
38 M. Usman, M. Adnan, M. T. Ahsan, S. Javed, M. S. Butt and M. A. Akram, *ACS Omega*, 2021, **6**, 1190–1196.
39 E. A. Alabdullkarem and J. Khan, *RSC Adv.*, 2025, **15**, 24831–24843.
40 Y. Mei, H. Li, Y. Cong, S. Huang, W. Xu, J. Qian and T.-T. Li, *Int. J. Hydrogen Energy*, 2021, **46**, 36046–36055.
41 B. Ricciardi, W. da Silva Freitas, B. Mecheri, K. U. Nisa, J. Montero, V. C. A. Ficca, E. Placidi, C. Alegre and A. D'Epifanio, *Carbon*, 2024, **219**, 118781.
42 A. Mezza, M. Bartoli, A. Chiodoni, J. Zeng, C. F. Pirri and A. Sacco, *Nanomaterials*, 2023, **13**, 2314.
43 A. Radecka, P. A. J. Bagot, T. L. Martin, J. Coakley, V. A. Vorontsov, M. P. Moody, H. Ishii, D. Rugg and D. Dye, *Acta Mater.*, 2016, **112**, 141–149.
44 S. Boudjelida, X. Li, S. Djellali, G. Chiappetta, F. Russo, A. Figoli and M. Carraro, *Materials*, 2024, **17**, 2941.
45 M. M. Kamel, E. Alzahrani, I. S. Ibrahim and S. M. Rashwan, *Int. J. Electrochem. Sci.*, 2021, **16**, 210942.
46 A. B. Rohom, P. U. Londhe, S. K. Mahapatra, S. K. Kulkarni and N. B. Chaure, *High Perform. Polym.*, 2014, **26**, 641–646.
47 G. M. do Nascimento and M. L. A. Temperini, *J. Raman Spectrosc.*, 2008, **39**, 772–778.
48 W. Zhong, W. Li, C. Yang, J. Wu, R. Zhao, M. Idrees, H. Xiang, Q. Zhang and X. Li, *J. Energy Chem.*, 2021, **61**, 236–242.
49 M. Ayachi, F. Ayad, A. Djelloul, S. Sali, S. Anas, M. Guezzoul, L. Benharrat, L. Zougar and S. Kermadi, *J. Sol-Gel Sci. Technol.*, 2024, **110**, 503–517.
50 A. Niilisk, M. Moppel, M. Pärs, I. Sildos, T. Jantson, T. Avarmaa, R. Jaaniso and J. Aarik, *Open Phys.*, 2006, **4**, 105–116.
51 M. Jung and Y.-W. Choi, *Appl. Surf. Sci.*, 2021, **554**, 149636.
52 J. El Nady, A. Shokry, M. Khalil, S. Ebrahim, A. M. Elshaer and M. Anas, *Sci. Rep.*, 2022, **12**, 3611.
53 Y. Meng, K. Wang, Y. Zhang and Z. Wei, *Adv. Mater.*, 2013, **25**, 6985–6990.
54 Md. T. Islam, S. Islam, G. M. G. Hossain, D. Islam and P. K. Bakshi, *J. Inorg. Organomet. Polym.*, 2025, **35**, 5563–5577.
55 L. H. Grey, H.-Y. Nie and M. C. Biesinger, *Appl. Surf. Sci.*, 2024, **653**, 159319.
56 A. Perumal, R. Kanumuri, S. K. Rayala and R. Nallaiyan, *J. Mater. Sci.*, 2020, **55**, 15602–15620.
57 Md. G. Azam, M. H. Kabir, Md. A. A. Shaikh, S. Ahmed, M. Mahmud and S. Yasmin, *J. Water Process Eng.*, 2022, **46**, 102597.
58 S. Yasmin, M. H. Kabir, N. Roy and S. Jeon, *ECS Adv.*, 2023, **2**, 024504.
59 S. Yasmin, M. H. Kabir, M. A. A. Shaikh and S. Jeon, *ECS J. Solid State Sci. Technol.*, 2023, **12**, 111004.
60 S. Yasmin, S. Cho and S. Jeon, *Appl. Surf. Sci.*, 2018, **434**, 905–912.
61 M. Sakil, M. H. Kabir, Md. A. Jabbar, Md. S. Hossain, A. M. Kusum, T. Jahan, M. Shahriar Bashar and S. Yasmin, *ACS Appl. Nano Mater.*, 2025, **8**, 22722–22735.
62 N. Roy, S. Yasmin, A. Ejaz, H. Soon Han and S. Jeon, *Appl. Surf. Sci.*, 2020, **533**, 147500.
63 S. Yasmin, M. S. Ahmed, D. Park and S. Jeon, *J. Electrochem. Soc.*, 2016, **163**, B491.
64 S. Yasmin, M. S. Ahmed and S. Jeon, *J. Electrochem. Soc.*, 2015, **162**, B363.
65 B. P. Upoma, S. Yasmin, Md. A. Ali Shaikh, T. Jahan, Md. A. Haque, M. Moniruzzaman and M. H. Kabir, *ACS Omega*, 2022, **7**, 29655–29665.
66 M. S. Hossain, M. H. Kabir, M. A. A. Shaikh, M. A. Haque and S. Yasmin, *RSC Adv.*, 2024, **14**, 1431–1444.
67 F. Mojumder, S. Yasmin, M. A. A. Shaikh, P. Chowdhury and M. H. Kabir, *J. Hazard. Mater. Adv.*, 2024, **14**, 100429.
68 S. Yasmin, M. S. Ahmed and S. Jeon, *J. Nanosci. Nanotechnol.*, 2017, **17**, 3959–3966.
69 L. Soriano, I. Preda, A. Gutiérrez, S. Palacin, M. Abbate and A. Vollmer, *Phys. Rev. B*, 2007, **75**, 233417.
70 B. Payne, M. Biesinger and N. Mcintyre, *J. Electron Spectrosc. Relat. Phenom.*, 2009, **175**, 55–65.
71 S. Petitto and M. Langell, *J. Vac. Sci. Technol., A*, 2004, **22**, 1690–1696.
72 A. Gunasekaran, P. Muthukumar, D. Govindan, M. Mariappan, M. Pannippara, A. Al-sehemi and S. Anthony, *New J. Chem.*, 2024, **48**, 1671–1677.
73 S. Jiang, B. Yi, H. Zhang, W. Song, Y. Bai, H. Yu and Z. Shao, *ChemElectroChem*, 2016, **3**, 734–740.
74 T. Hao, Y. Liu, G. Liu, C. Peng, B. Chen, Y. Feng, J. Ru and J. Yang, *Energy Storage Mater.*, 2019, **23**, 225–232.
75 F. Ziaeimoghaddam and R. Arefinia, *Prog. Org. Coat.*, 2022, **170**, 106952.
76 X. Chu, W. Yang and H. Li, *Mater. Horiz.*, 2023, **10**, 670–697.
77 S. Palsaniya, H. B. Nemade and A. K. Dasmahapatra, *J. Phys. Chem. Solids*, 2021, **154**, 110081.
78 X. Lu, G. Wang, T. Zhai, M. Yu, J. Gan, Y. Tong and Y. Li, *Nano Lett.*, 2012, **12**, 1690–1696.

79 C. Li, J. Xu, Q. Xu, G. Xue, H. Yu, X. Wang, J. Lu, G. Cui and G. Gu, *Prog. Org. Coat.*, 2022, **165**, 106673.
80 K.-U. Lee, J. Y. Byun, H.-J. Shin and S. H. Kim, *J. Alloys Compd.*, 2019, **779**, 74–80.
81 K. Li, X. Liu, S. Chen, W. Pan and J. Zhang, *J. Energy Chem.*, 2019, **32**, 166–173.
82 S. A. Ansari, N. A. Khan, Z. Hasan, A. A. Shaikh, F. K. Ferdousi, H. R. Barai, N. S. Lopa and M. M. Rahman, *Sustainable Energy Fuels*, 2020, **4**, 2480–2490.
83 R. Kumar, B. K. Singh, A. Soam, S. Parida, V. Sahajwalla and P. Bhargava, *Nanoscale Adv.*, 2020, **2**, 2376–2386.
84 W. Li, J. Hao, S. Mu and W. Liu, *Appl. Surf. Sci.*, 2020, **507**, 144889.
85 X. Zheng, Z. Gu, Q. Hu, B. Geng and X. Zhang, *RSC Adv.*, 2015, **5**, 17007–17013.
86 S. B. Aziz, E. M. A. Dannoun, A. R. Murad, K. H. Mahmoud, M. A. Brza, M. M. Nofal, K. A. Elsayed, S. N. Abdullah, J. M. Hadi and M. F. Z. Kadir, *Alexandria Eng. J.*, 2022, **61**, 5919–5937.
87 K. J. Aoki, J. Chen, Y. Liu and B. Jia, *J. Electroanal. Chem.*, 2020, **856**, 113609.
88 T. S. Mathis, N. Kurra, X. Wang, D. Pinto, P. Simon and Y. Gogotsi, *Adv. Energy Mater.*, 2019, **9**, 1902007.
89 P. Simon and Y. Gogotsi, *Nat. Mater.*, 2008, **7**, 845–854.
90 O. Saha, Md. H. Kabir, Md. M. Islam, Md. S. Hossain, M. S. Bashar, M. Y. Pabel and S. Yasmin, *RSC Adv.*, 2025, **15**, 41874–41885.
91 D. Jhankal, M. S. Khan, P. Shakya, N. Bhardwaj, B. Yadav, K. K. Jhankal and K. Sachdev, *Energy Adv.*, 2024, **3**, 191–202.
92 Md. A. Hasan and Md. M. Islam, *J. Energy Storage*, 2024, **98**, 113015.
93 M. Yu, X. Cheng, Y. Zeng, Z. Wang, Y. Tong, X. Lu and S. Yang, *Angew. Chem.*, 2016, **128**, 6874–6878.
94 R. D. Oliveira, C. S. Santos, J. R. Garcia, M. Vidotti, L. F. Marchesi and C. A. Pessoa, *J. Electroanal. Chem.*, 2020, **878**, 114662.
95 I. Beyers, A. Bensmann and R. Hanke-Rauschenbach, *J. Energy Storage*, 2023, **73**, 109097.
96 C. Choi, D. S. Ashby, D. M. Butts, R. H. DeBlock, Q. Wei, J. Lau and B. Dunn, *Nat. Rev. Mater.*, 2020, **5**, 5–19.
97 A. Eftekhari and M. Mohamedi, *Mater. Today Energy*, 2017, **6**, 211–229.
98 A. Said, B. Qian, R. Zhang, C. Yang, K. Xu, K. Chen and D. Xue, *J. Mater. Chem. A*, 2025, **13**, 6469–6481.
99 A. Ch. Lazanas and M. I. Prodromidis, *ACS Meas. Sci. Au*, 2023, **3**, 162–193.
100 R. Li, Z. Hu, X. Shao, P. Cheng, S. Li, W. Yu, W. Lin and D. Yuan, *Sci. Rep.*, 2016, **6**, 18737.
101 X. Ge, Y. He, T. Plachy, N. Kazantseva, P. Saha and Q. Cheng, *Nanomaterials*, 2019, **9**, 527.
102 J.-K. Chih, A. Jamaluddin, F. Chen, J.-K. Chang and C.-Y. Su, *J. Mater. Chem. A*, 2019, **7**, 12779–12789.
103 Md. A. Rahman, Md. A. Haque, Md. A. A. Shaikh, C. K. Roy, A. H. Reaz, Md. T. A. Shawon, P. K. Baksi, S. Yasmin, M. H. Kabir, S. H. Won, T. W. Kim and Md. M. Rahman, *J. Energy Storage*, 2024, **99**, 113205.
104 Z. Li, X. Deng, G. Chen, Z. Zhang, J. Han and X. Lu, *Chem. Eng. J.*, 2025, **524**, 169372.
105 P. Zhang, Z. Liu, Y. Liu, H. Fan, Y. Jiao and B. Chen, *Electrochim. Acta*, 2015, **184**, 1–7.